The Astrophysical Journal Letters, 1002:L17 (11pp), 2026 May 1 https://doi.org/10.3847/2041-8213/ae5c9f


# Mature but Still Growing: JWST Detection of the Earliest Intracluster Light at $z \sim 2$

Hyungjin Joo[1], M. James Jee[1,2], Kyle Finner[3], Zachary P. Scofield[1], Sangjun Cha[1], Jinhyub Kim[4], Ranga-Ram Chary[5], Andreas Faisst[3], and Bomee Lee[6]
[1] Department of Astronomy, Yonsei University, 50 Yonsei-ro, Seoul 03722, Republic of Korea; gudwls4478@yonsei.ac.kr, mkjee@yonsei.ac.kr
[2] Department of Physics and Astronomy, University of California, Davis, One Shields Avenue, Davis, CA 95616, USA
[3] IPAC, California Institute of Technology, 1200 East California Boulevard, Pasadena, CA 91125, USA
[4] Department of Physics, University of Oxford, Denys Wilkinson Building, Keble Road, Oxford OX1 3RH, UK
[5] University of California, Los Angeles, CA 90095-1562, USA
[6] Korea Astronomy and Space Science Institute, 776 Daedeokdae-ro, Yuseong-gu, Daejeon 34055, Republic of Korea
*Received 2026 March 3; revised 2026 April 4; accepted 2026 April 6; published 2026 April 22*

## Abstract

We present a JWST analysis of intracluster light (ICL) in XLSSC 122 at $z = 1.98$, currently the most distant known strong-lensing galaxy cluster with an evolved member population. Using deep JWST imaging complemented by Hubble Space Telescope data and careful control of systematics, we robustly detect diffuse emission extending to several hundred kiloparsecs from the brightest cluster galaxy (BCG) down to $\sim$29 mag arcsec$^{-2}$. Multicomponent point-spread-function-convolved Sérsic modeling separates the surface brightness profiles into three components: a BCG core, a BCG envelope, and an ICL component, with stable Sérsic indices across wavelengths. Nearly flat color profiles indicate minimal radial variation in the stellar populations of the BCG envelope and the ICL. The median ICL fraction measured across seven bands is $\sim$17%, demonstrating that the buildup of intracluster stars in massive halos was already well underway by $z \sim 2$. The ICL fraction peaks near 5000 Å in the rest frame, which provides the first confirmation at $z > 1$ that this characteristic rise is a feature of dynamically active clusters. We also detect a southern excess of ICL relative to the best-fit Sérsic model and quantify it using wavelet-based modeling, providing additional support that this system is dynamically active. The BCG + ICL light distribution and strong-lensing mass map show strong morphological agreement within $\sim$100 kpc. These findings establish the ICL as an early forming and dynamically informative component of massive halos.

*Unified Astronomy Thesaurus concepts:* High-redshift galaxy clusters (2007); Galaxy clusters (584); Hubble Space Telescope (761); James Webb Space Telescope (2291); Dark matter (353); Galaxy interactions (600)

## 1. Introduction

Intracluster light (ICL) was first reported by F. Zwicky (1937) as faint emission between galaxies in the Coma Cluster. Since then, decades of studies have revealed that ICL constitutes a significant stellar component in galaxy clusters. The ICL is composed of stars that are unbound from cluster galaxies and provides unique insights into galaxy evolution and the assembly history of massive structures.

The physical explanation for the formation of the ICL remains in contention. Some studies attribute most of the ICL to the formation of the brightest cluster galaxy (BCG) through mergers or violent relaxation (e.g., G. Murante et al. 2007; J. Ko & M. J. Jee 2018), while others emphasize satellite tidal stripping (e.g., C. S. Rudick et al. 2009; E. Contini et al. 2019) or preprocessing in galaxy groups prior to cluster accretion (e.g., C. S. Rudick et al. 2006; E. Contini et al. 2014). Recent studies with cosmological simulations suggest that these channels are not mutually exclusive but instead form a continuous sequence. While multiple mechanisms contribute simultaneously to ICL buildup, the dominant driver varies by system based on its unique evolutionary history (H. Joo et al. 2025).



Observational and theoretical studies suggest that the ICL can provide valuable information on cluster assembly history. The ICL has been shown to be a sensitive tracer of the global dark-matter distribution in clusters (e.g., M. J. Jee 2010; M. Montes & I. Trujillo 2019; J. Yoo et al. 2024; J. Butler et al. 2025; S. Cha et al. 2025). Furthermore, A. J. Deason et al. (2021) and A. H. Gonzalez et al. (2021) emphasized the potential of the ICL as a diagnostic for identifying the splashback radius in clusters. Beyond tracing dark matter, the ICL also provides valuable constraints on the dynamical state of clusters. Recent studies suggest that the observed ICL fraction is a nearly constant function of wavelength in relaxed clusters, whereas unrelaxed systems tend to show a higher overall ICL fraction and a modest increase in the ICL fraction around 4800 Å (e.g., Y. Jiménez-Teja et al. 2018, 2021; N. O. L. de Oliveira et al. 2022, 2025). This enhancement in both the total ICL content and the blue spectral component likely reflects the contribution of recently stripped young stars during active merging events. Simulations further demonstrate that the asymmetric spatial distribution of the ICL becomes more prominent when the host halo is not fully virialized (e.g., K. Chun et al. 2024; H. Joo et al. 2025; L. C. Kimmig et al. 2025; S. Jeon et al. 2026). Together, these properties make the ICL a powerful probe of cluster dynamical states and a unique test of hierarchical structure formation in the ΛCDM paradigm.

Because the ICL is accumulated over a wide range of epochs (e.g., H. J. Brown et al. 2024; E. Contini et al. 2024;

H. Joo et al. 2025; S. Jeon et al. 2026), it preserves a cumulative record of past interactions and accretion events in clusters. Unlike gas or galaxies, which can dynamically relax or dissipate on relatively short timescales, the diffuse stellar component retains imprints of the cluster's assembly over several gigayears (G. Murante et al. 2007; C. S. Rudick et al. 2009). The spatial and structural properties of the ICL thus may provide a fossil record of hierarchical growth, offering a long-term view of how stellar material is redistributed within massive halos.

Probing the ICL at high redshift has long been challenging due to its extremely low surface brightness (SB). Thanks to the Hubble Space Telescope (HST), observations have extended to $z \sim 1$–2 (e.g., T. DeMaio et al. 2018; H. Joo & M. J. Jee 2023), but they are limited by depth and wavelength coverage. For clusters at $z > 2$, optical observations probe rest-frame wavelengths shortward of the Balmer break, where the ICL emission drops steeply. Therefore, even at comparable SB limits, optical data generally lack the signal needed to trace the diffuse light reliably. Unlike HST, which is limited to observations at wavelengths up to 1.7 $\mu$m, JWST probes significantly longer wavelengths, making it a powerful tool for studying the ICL at $z \gtrsim 2$. The unprecedented infrared sensitivity of JWST now enables direct detections of diffuse stellar halos in more distant clusters.

In this context, XLSSU J021744.1-034536 (hereafter XLSSC 122, $z = 1.98$) stands out as one of the most distant massive clusters observed to date (M. Pierre et al. 2006, 2016; J. P. Willis et al. 2013, 2020; K. Finner et al. 2025; J. Kim et al. 2025; Z. P. Scofield et al. 2026). With a look-back time of $\sim$10 Gyr, it provides a unique laboratory to test how early massive halos assembled their stellar and dark-matter components. Although several galaxy overdensities at comparable redshifts have been reported (e.g., D. D. Shi et al. 2024; H. Sun et al. 2024; R. Shimakawa et al. 2025), these systems are often interpreted as being in a protocluster stage. In contrast, previous studies have shown that XLSSC 122 is already a mature, gravitationally bound cluster. Spectroscopic observations identified 37 member galaxies and indicated evolved stellar populations (J. P. Willis et al. 2020), while HST data reveal a quiescent fraction ($\sim$88% within $0.5r_{500}$) significantly above the typical field value of $\sim$20% at $z \sim 2$ (E. Noordeh et al. 2021). The cluster also hosts an extended, hot intracluster medium (A. B. Mantz et al. 2018). Mass estimates range from $M_{500} = (6.3 \pm 1.5) \times 10^{13}\,M_{\odot}$ via X-ray analysis (A. B. Mantz et al. 2018) to $M_{200,c}$ values of $(3.3 \pm 1.8) \times 10^{14}\,M_{\odot}$ from HST weak lensing (J. Kim et al. 2025), $(2.6 \pm 1.1) \times 10^{14}\,M_{\odot}$ from JWST strong lensing (SL; K. Finner et al. 2025), and $(1.6 \pm 0.3) \times 10^{14}\,M_{\odot}$ from JWST weak lensing (Z. P. Scofield et al. 2026). Despite this maturity, multiwavelength evidence indicates that XLSSC 122 is dynamically active. The Sunyaev–Zel'dovich (SZ) signal exhibits a southern excess and is offset from the BCG and X-ray peaks (J. van Marrewijk et al. 2023). Recent JWST weak-lensing analyses confirm this spatial offset between the SZ signal and the mass and X-ray centers, strongly pointing to ongoing merger activity (Z. P. Scofield et al. 2026).

In this Letter, we present an analysis of the ICL in XLSSC 122 using HST and JWST observations. The combination of deep JWST imaging and SL constraints (K. Finner et al. 2025) now enables the first detailed study of the cluster's extended diffuse stellar light and the relationship between its ICL and dark matter. We find that this system exhibits a high ICL fraction, comparable to those of low-redshift clusters, and demonstrate that spatial and color variations offer insights into its dynamical state. Section 2 describes the observations and detailed data reduction. Section 3 presents the results of the BCG and ICL decomposition and measurements of the ICL fraction. Section 4 discusses the asymmetric ICL feature and a comparison with the SL mass map, and Section 5 summarizes the main results. We report magnitudes in the AB system and adopt a flat $\Lambda$CDM cosmology with $H_0 = 70\,\mathrm{km\,s^{-1}\,Mpc^{-1}}$ and $\Omega_M = 0.3$ throughout this Letter. At the cluster redshift ($z = 1.98$), this cosmology provides an angular scale of $1'' = 8.379$ kpc.

## 2. Data and Method

### 2.1. Data Reduction

In this work, we analyze HST and JWST observations of XLSSC 122. The HST data used in this analysis were obtained in three filters (F814W, F105W, and F140W; Program IDs 15267 and 17172; PI: R. E. A. Canning). The JWST imaging consists of four filters (F090W, F200W, F277W, and F356W; Program ID 3950; PI: K. Finner). The average SB limit of the JWST imaging is $\sim$29.2 mag arcsec$^{-2}$, while diffuse ICL is expected to appear at $\mu \sim 28$ mag arcsec$^{-2}$ at $z \sim 2$.[7] This depth ensures that the JWST data are sufficiently deep to robustly detect the ICL at this redshift and enable reliable cross-filter comparisons.

While initial reduction of the HST and JWST data followed standard calibration pipelines, we employed custom pipelines to address specific systematics critical to ICL analysis. The HST observations were reduced using `AstroDrizzle` in the `DrizzlePac` package (S. L. Hoffmann et al. 2021). The JWST data were processed with the standard JWST calibration pipeline (H. Bushouse et al. 2022). Both the HST and JWST mosaics were resampled to a common pixel scale of $0.''02\,\mathrm{pixel^{-1}}$ using a square drizzle kernel. Several systematics, such as wisp features, $1/f$ noise, sky gradients, and residual background, were corrected using customized postprocessing routines for HST (H. Joo & M. J. Jee 2023) and JWST[8] (Z. P. Scofield 2025), respectively. For wisp features, we adopted version 3 of Wisp Templates[9] provided by the JWST User Documentation, which has $\sim$50% less noise than version 2.[10] Further details on customized data reduction procedures are described in Appendix A. These steps reduce instrumental systematics, which are particularly important for robust SB measurements of diffuse emission.

ICL analysis is sensitive to large-scale flux variations. Current in-flight calibrations have reduced large-scale flat-field systematic residuals (L-flats) to $\lesssim$1% across the NIRCam detectors (B. Sunnquist et al. 2024). At this level of precision, the dominant systematics are no longer the flat-field response, but rather detector-level artifacts like $1/f$ noise and scattered light wisps, which we address through our custom pipeline mentioned above.

[7] This estimate assumes a local ($z = 0$) SB of $\mu_V \sim 26.5$ mag arcsec$^{-2}$, scaled for cosmological dimming, the $k$-correction, and stellar evolution.

[8] https://github.com/zpscofield/young-jwstpipe

[9] https://stsci.box.com/s/1bymvf1lkrqbdn9rnkluzqk30e8o2bne

[10] https://www.stsci.edu/contents/news/jwst/2024/new-nircam-wisp-templates-are-now-available

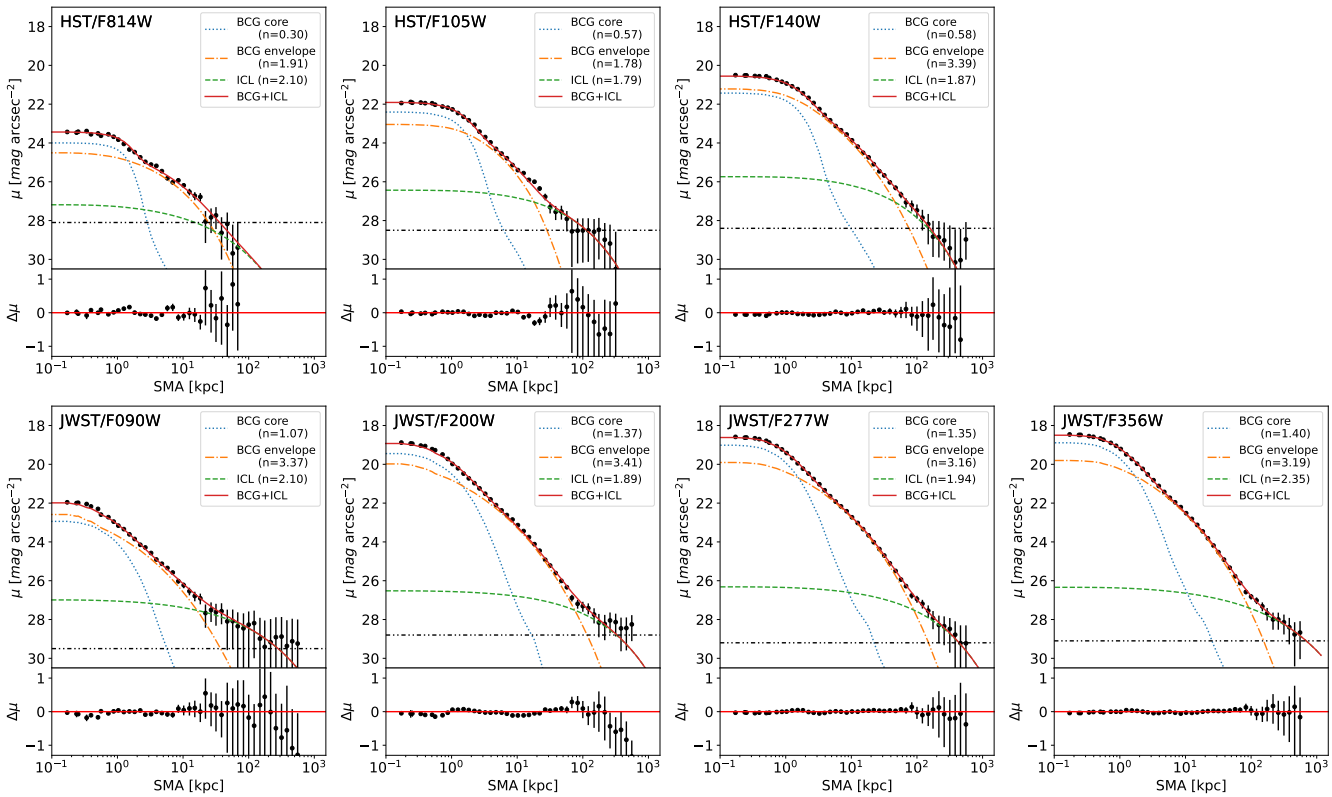


**Figure 1.** Multiband SB profiles and model decomposition. The top row displays HST observations (F814W, F105W, and F140W), while the bottom row presents JWST/NIRCam observations (F090W, F200W, F277W, and F356W). Black data points represent the observed median SB within elliptical bins, with error bars accounting for the quadrature sum of flux uncertainties and systematic sky error ($\sigma_{\rm sky}$). Horizontal dotted–dashed lines indicate the limiting SB ($\mu_{\rm lim}$) for each respective band. The red solid line denotes the best-fit multicomponent Sérsic model convolved with the telescope point-spread function (PSF). The model is decomposed into three distinct stellar components: the BCG core (blue dotted line), the BCG envelope (orange dotted–dashed line), and the diffuse ICL (green dashed line). The last components (green dashed line) are utilized for the ICL analysis in this work. Lower subpanels show the residuals ($\Delta\mu$) between the observed data and the total model.

### 2.2. Surface Brightness Measurement

Before measuring the SB profiles of the BCG and ICL, we masked out all discrete sources. A mask map was constructed using the segmentation map generated by `SExtractor`. To further minimize the influence of extended sources, the mask map was expanded using a binary dilation method (G. Matheron 1988). The expansion width ($w$) for each source was scaled individually using the following relation:

$$w = c_{\rm e} \times r_{\rm m}, \quad (1)$$

where $c_{\rm e}$ is the expansion coefficient, and $r_{\rm m}$ is the radius derived from the area of the original segmentation mask, defined as $r_{\rm m} = \sqrt{\rm area/\pi}$. While H. Joo & M. J. Jee (2023) used the half-light radius of each source, this approach was replaced by $r_{\rm m}$ in this work to better handle bright stellar sources, which are not well represented by half-light radii. We adopted $c_{\rm e} = 1.2$ to minimize contamination from other light sources while avoiding excessive masking of the ICL. The BCG itself was excluded from the masking process to preserve its flux profile.

After applying the masks, we defined elliptical bins centered on the BCG that matched the elongated BCG + ICL morphology. The global ellipticity and position angle, accounting for both the BCG and ICL, were measured using `AUTOPROF` (C. J. Stone et al. 2021) from the detection image constructed by combining the four JWST filters (F090W, F200W, F277W, and F356W). We obtained a global ellipticity ($1 - b/a$) of $0.458 \pm 0.011$ and a position angle of $102.^{\circ}3 \pm 0.^{\circ}288$, measured counterclockwise from the east. Using a background region outside the 1 Mpc ellipse, we estimated the SB limits, $\mu_{\rm lim}$, and the sky estimation uncertainties, $\sigma_{\rm sky}$, for each band (Appendix A.2). The elliptical radial bins were defined with the semimajor axis (SMA) increasing logarithmically. We estimated the median SB level within each bin and its associated measurement error. The errors were estimated by adding the flux uncertainties and $\sigma_{\rm sky}$ within each radial bin in quadrature. The radial SB profiles are presented in Figure 1 for all seven bands.

Color profiles are a useful tool for comparing the stellar populations of the BCG and the ICL. We constructed color profiles from the SB profiles of adjacent filter pairs so as to trace the local slope of the underlying spectral energy distribution (SED) more directly. Figure 2 shows color profiles constructed from the six adjacent filter pairs: F814W − F090W, F090W − F105W, F105W − F140W, F140W − F200W, F200W − F277W, and F277W − F356W, following the wavelength-ordered sequence of the filters. The uncertainty in each color profile was calculated by adding the uncertainties in the two SB profiles in quadrature. A discussion of the results is presented in Section 3.1.

## 3. Results

### 3.1. Radial Profiles of the Brightest Cluster Galaxy and Intracluster Light

As shown in Figure 1, the ellipsoidal profiles reveal the existence of diffuse stellar light beyond a few hundred

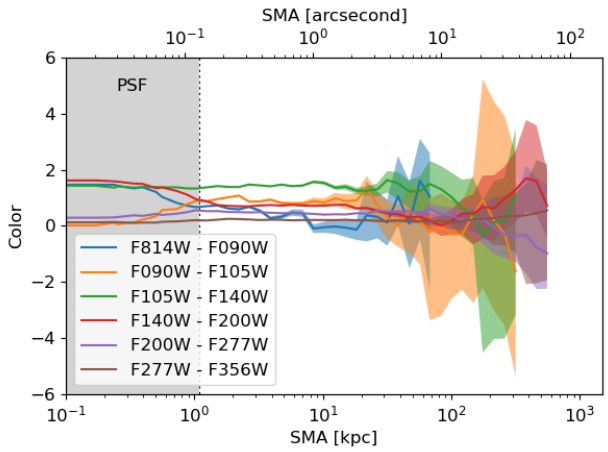


**Figure 2.** Radial color profiles of the BCG + ICL derived from six adjacent filter pairs. Shaded regions represent the 68% confidence interval, incorporating both statistical flux uncertainties and systematic sky background errors ($\sigma_{\rm sky}$). The inner gray region ($\lesssim$1 kpc) indicates the area where differences in PSF widths between HST and JWST may induce artificial color gradients. Beyond this scale, the color profiles remain remarkably flat within the error margins, suggesting a spatially uniform stellar population across the BCG envelope and ICL. A notable exception is the F814W − F090W profile, which exhibits variation at $3 \lesssim$ SMA $\lesssim 10$ kpc, potentially indicating radial differences such as dust attenuation within the central galaxy (see text).

kiloparsecs from the BCG in most bands, thereby enabling direct constraints on the spatial extent of the diffuse stellar component at $z \sim 2$. In F814W, which probes rest-frame wavelengths blueward of the Balmer break ($\sim$3645 Å), the diffuse emission appears weaker than in the other bands. While F090W and F814W cover a similar spectral range, F090W's higher throughput at longer wavelengths, combined with NIRCam's high sensitivity, extends our detection of the ICL to greater radial distances from the BCG, despite its shorter exposure time. In both HST and JWST images, the diffuse signal strengthens toward longer wavelengths, consistent with emission from evolved stars and the scarcity of young, blue stars in the ICL at $z \sim 2$.

To quantify the contributions of the ICL to these profiles, we decomposed the SB profiles into multiple components as described below. We assumed that each component follows a Sérsic profile (J. L. Sérsic 1963) and modeled the overall profile as a sum of Sérsic functions, as shown in Equation (2):

$$\mu(R) = \mathrm{PSF}(R) * \sum_{i}^{N} I_{\mathrm{e},i} \exp \times \left[ -k\left( \left( \frac{R}{R_{\mathrm{e},i}} \right)^{1/n_i} - 1 \right) \right]. \quad (2)$$

Here, the model is convolved with the PSF to account for both the blurring effect and diffraction spikes. We used `TinyTim` (J. E. Krist et al. 2011) to simulate the PSF of HST and `STPSF` (M. D. Perrin et al. 2014) for JWST.

Before decomposing the BCG and ICL, we determined the number of required Sérsic components. First, we calculated the Bayes factor ($K$) by comparing the evidence value of two different models: two-component and three-component Sérsic models. $K_{32}$ is defined as in Equation (3):

$$K_{32} = \frac{\Pr(D|M_3)}{\Pr(D|M_2)}, \quad (3)$$

where $D$ denotes the observed data, and $M_2$ and $M_3$ correspond to two- and three-component models, respectively. We used `PyMultiNest` (J. Buchner et al. 2014) to obtain the evidence for each model. The resulting $\log_{10}(K_{32})$ values are 0.58 (F814W), 1.22 (F105W), 1.16 (F140W), 1.10 (F090W), 1.02 (F200W), 1.24 (F277W), and 1.05 (F356W). According to Jeffreys' scale (H. Jeffreys 1998), the three-component model is "substantially" preferred to the two-component model for the F814W profile, even though the profile reaches its limiting depth at $\sim$50 kpc. For the other bands, the three-component models are "strongly" favored with Bayes factors greater than 10. Thus, we adopted three Sérsic components to model the BCG and ICL profiles. Figure 1 presents the results of the three-component modeling with `PyMultiNest`.

To further validate the requirement of three components, we examined additional independent criteria proposed in previous studies. The BCG–ICL transition was identified from the curvature of the 2D light distribution by Y. Jiménez-Teja & R. Dupke (2016). A. H. Gonzalez et al. (2021) showed that a corresponding signature can also be seen as a dip in the derivative of the SB profile, typically found on scales of several tens of kiloparsecs, consistent with both simulations (e.g., E. Contini et al. 2022) and observations (e.g., M. Montes & I. Trujillo 2017). Building on this approach, H. Joo & M. J. Jee (2023) proposed using the number of such dips as an indicator of the number of Sérsic components, adopting one more component than the number of detected dips. Similarly, Y. Zhang et al. (2019) found that three Sérsic components were required to reproduce stacked Dark Energy Survey cluster profiles. In our data, we identified two dips in the SB profiles for six filters, except for F814W. The consistency between the dip-based expectations and Bayes factor selection therefore provides an independent check on our adopted three-component decomposition.

In the F814W band, we do not attribute the single dip to the BCG–ICL transition, as it occurs at merely $\sim$10 kpc, significantly inward of the transition radii observed in the other filters. We infer that the F814W SB profile lacks sufficient signal-to-noise ratio (S/N) to probe the true BCG–ICL transition region based on dip detection scheme. Consequently, a two-component fit in this band would model the BCG core and an artificially extended envelope rather than achieving a clean BCG–ICL separation. Furthermore, the Bayes factor indicates that this two-component scenario is statistically disfavored compared to the three-component model.

Figure 2 presents the color profiles of the BCG and the ICL across the six filter combinations. Beyond $\sim$10 kpc, all six colors exhibit nearly flat radial gradients, indicating little change in the stellar populations with distance from the center. At SMA $\lesssim$ 3 kpc, radial color trends appear in the F814W – F090W, F090W – F105W, and F140W – F200W colors. These colors are constructed from filters observed with different telescopes and therefore have substantially different PSF widths (e.g., $\sim$0.″08 for F814W and $\sim$0.″03 for F090W), suggesting that the trends are likely to be driven by PSF mismatch rather than stellar population differences. A noticeable

variation is detected only in F814W – F090W at $3 \lesssim \mathrm{SMA} \lesssim 10$ kpc, corresponding to the BCG-dominated region. Because this color corresponds to the rest-frame near-ultraviolet, the observed behavior likely indicates intrinsic properties of the central galaxy, such as dust attenuation. Further analysis of the BCG is required to identify the physical driver of this variation.

Meanwhile, the Sérsic indices are broadly consistent across the seven bands: the BCG cores are approximately exponential ($n \sim 1$), the BCG envelopes show steeper profiles with $n \sim 3$, and the ICL components remain relatively diffuse with $n \sim 2$. Although this cluster is located at $z = 1.98$, the profile decomposition reveals a structure similar to the stacked profiles at $z \sim 0.25$ reported by Y. Zhang et al. (2019). Taken together, these results indicate that the BCG and ICL in XLSSC 122 have already settled into a smooth, extended structure by $z \sim 2$. If we consider the mass of this halo ($M_{200,c} = 2.6 \pm 1.1 \times 10^{14}\, M_{\odot}$ from SL modeling; K. Finner et al. 2025), the presence of a mature structure is not unexpected (e.g., E. Contini et al. 2024; H. Joo et al. 2025; L. C. Kimmig et al. 2025). These findings establish XLSSC 122 as the earliest cluster in which the structural maturity of the ICL can be directly characterized.

### 3.2. Intracluster Light Fraction

Based on the Sérsic decomposition, we next measured the ICL flux fraction at each wavelength. We define the ICL fraction as follows:

$$f_{\mathrm{ICL}} = \frac{F_{\mathrm{ICL}}}{F_{\mathrm{ICL}} + F_{\mathrm{galaxy}}}, \tag{4}$$

where $F_{\mathrm{galaxy}}$ denotes the flux from XLSSC 122 member galaxies, including the BCG, selected via either spectroscopic or photometric criteria (see Appendix B). For each filter, $F_{\mathrm{galaxy}}$ and $F_{\mathrm{ICL}}$ are estimated within the specific radius where the SB profile intersects the limiting magnitude ($\mu_{\mathrm{lim}}$). This criterion ensures that the ICL is measured only in regions with sufficient S/N, thereby avoiding biases from extrapolated signals. The ICL fractions measured out to the limiting radius in each band are 11.4% ± 0.45% within 21.9 kpc (F814W), 18.0% ± 2.98% within 68.5 kpc (F105W), 23.4% ± 1.04% within 177.6 kpc (F140W), 16.6% ± 2.13% within 267.2 kpc (F090W), 13.1% ± 0.94% within 319.4 kpc (F200W), 16.6% ± 1.65% within 460.7 kpc (F277W), and 19.8% ± 0.78% within 557.4 kpc (F356W). The average fraction in the seven bands is ∼17%.

Previous studies based on HST observations have provided constraints on the ICL fraction at $z \sim 2$. H. Joo & M. J. Jee (2023) reported an ICL fraction of approximately 10% in JKCS041 at $z = 1.9$. S. V. Werner et al. (2023) further showed that in systems at $z \sim 2$, such as CARLA J1018+053, the ICL component appears to be strongly concentrated toward the central regions. However, due to the limited wavelength coverage and sensitivity of HST, ICL measurements in systems at $z \gtrsim 2$ are restricted to small apertures near the BCGs. This study demonstrates that such limitations can be alleviated using JWST, enabling robust quantification of the ICL fraction at higher redshifts. Additionally, R. T. Coogan et al. (2023) reported an ICL fraction of approximately 10% in a protocluster at $z = 1.85$. While this value is slightly lower than that measured in this work, it remains consistent with the mass-dependent trend of ICL fraction suggested by R. J. Mayes et al. (2026) and H. Joo et al. (2025) from groups to clusters. This study indicates that the ICL fraction measured in massive halos at $z \sim 2$ is consistent with previous estimates based on HST observations. These results indicate that the buildup of the ICL fraction in massive galaxy clusters was already well established by $z \sim 2$, consistent with early assembly of diffuse stellar components.

## 4. Discussion

### 4.1. Wavelength Dependence of the Intracluster Light Fraction

Recent studies suggest that both the total amount and the wavelength dependence of the ICL fraction reflect the dynamical state of galaxy clusters. On average, merging or dynamically active systems exhibit higher ICL fractions than their relaxed counterparts. Furthermore, these dynamically disturbed clusters tend to show a characteristic rise in the ICL fraction near rest-frame 4800 Å, whereas relaxed systems display a comparatively flat trend across wavelengths (Y. Jiménez-Teja et al. 2018, 2021, 2025; N. O. L. de Oliveira et al. 2022, 2025).

Multiwavelength studies have suggested that XLSSC 122 might be an active system. Its SZ signal shows a southern excess and an offset from the BCG and X-ray peak (J. van Marrewijk et al. 2023). Recent JWST weak-lensing and multiwavelength analyses further reported an offset between the SZ and mass and X-ray peaks, pointing to ongoing merger activity (Z. P. Scofield et al. 2026). To investigate whether the ICL of XLSSC 122 follows the aforementioned trend, we studied the rest-frame wavelength dependence of the ICL fraction (Figure 3). The fraction remains relatively low below 3000 Å, increases toward a local maximum near 4800 Å, decreases up to ≈7000 Å, and increases again at longer wavelengths. The ICL fraction of XLSSC 122 shows a wavelength-dependent pattern broadly consistent with that observed in merging or dynamically disturbed clusters at lower redshifts. This suggests that this wavelength-based probe of dynamical state might hold even at $z \sim 2$.

According to Y. Jiménez-Teja et al. (2021), the enhanced ICL fraction around 4800 Å likely reflects the contribution from recently stripped young stars, whose bluer SEDs raise the measured fraction in dynamically active clusters. Y. Jiménez-Teja et al. (2024) further suggested that, in their merging clusters at $z > 0.8$, the $f_{\mathrm{ICL}}$ excess can be broader and shift to redder wavelengths, possibly reflecting a more assorted mixture of stellar populations inherited from the ICL that was mainly built through major mergers with the BCG at earlier epochs ($z > 1$). In XLSSC 122, the excess is closer in both peak location and width to the features in lower-redshift disturbed clusters. This suggests that the broader and redder excess identified by Y. Jiménez-Teja et al. (2024) may not be driven by redshift alone. Further studies over a wider redshift range are needed to clarify the origin of this diversity. At present, the observed structure in XLSSC 122 is consistent with the interpretation suggesting that tidal stripping and galaxy interactions are ongoing.

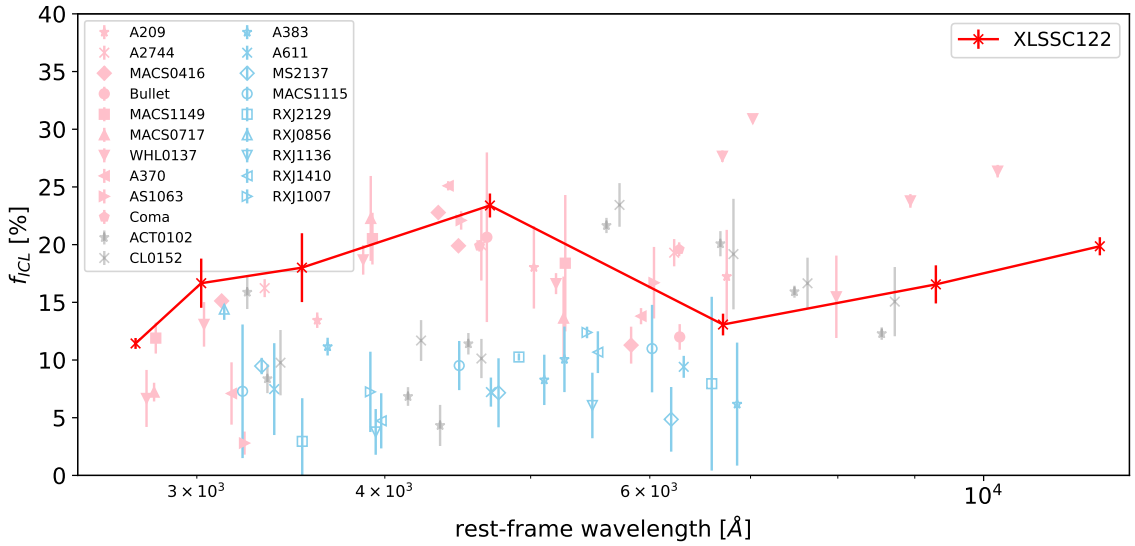


**Figure 3.** ICL fraction ($f_{\rm ICL}$) as a function of rest-frame wavelength. The red crosses represent the measurements for XLSSC 122 ($z = 1.98$) across the seven observed bands. For comparison, pink (sky blue) points indicate $f_{\rm ICL}$ in dynamically active (relaxed) clusters measured by Y. Jiménez-Teja et al. (2018, 2021, 2025) and N. O. L. de Oliveira et al. (2022, 2025). The gray points indicate the case of dynamically active at $z \sim 0.8$ (Y. Jiménez-Teja et al. 2024). The $f_{\rm ICL}$ values for XLSSC 122 exhibit a characteristic local maximum near 4800 Å, a pattern that closely resembles the trends found in dynamically active or merging systems.

### *4.2. Intracluster Light Excess Southward of the Brightest Cluster Galaxy*

Visual inspection of our JWST imaging data reveals an excess of diffuse emission near the member galaxies southward of the BCG. This feature is located at a projected distance of $\gtrsim$100 kpc from the BCG, and is still visible even after the subtraction of our Sérsic ICL model (i.e., outermost component). This signal is most significant in the F200W, F277W, and F356W filters, implying that its emission is dominated by a stellar population similar to that of the BCG and the ICL component in the Sérsic model. We show an image of XLSSC 122 after subtracting the 2D Sérsic model of ICL in the left column of Figure 4. This asymmetric excess departs from the symmetry expected from a relaxed ICL distribution. This offers observational support for the ICL substructure associated with dynamical activity in the central region.

To measure the flux of this southern ICL excess, we modeled the excess ICL with `DAWIS` (A. Ellien et al. 2021), an algorithm designed to detect the ICL with wavelets. The middle column of Figure 4 shows the model generated by `DAWIS`. The modeled ICL is distributed across the member galaxies south of the BCG. Nevertheless, identifying specific progenitor galaxies of this ICL component remains a challenge. Instead, the morphology of the excess broadly follows the southward elongation seen in the smoothed member density distribution (see the Appendix B). And we find no clear single massive galaxy counterpart at its location. These properties favor an origin in diffuse stellar debris produced by tidal stripping during recent galaxy interactions. Similar asymmetric ICL substructures are commonly found in simulations of dynamically unrelaxed clusters (e.g., H. Joo et al. 2025; S. Jeon et al. 2026).

The results of H. Joo et al. (2025) suggest that around 10% of the ICL in $z \sim 2$ or $M_{200} \geqslant 10^{14}\,M_{\odot}$ clusters is contributed by stars stripped from galaxies. In this study, the southern component accounts for $\sim$4% of the total ICL flux, defined as the sum of the Sérsic model ICL component and the southern ICL excess, in the three filters where it is most prominent.

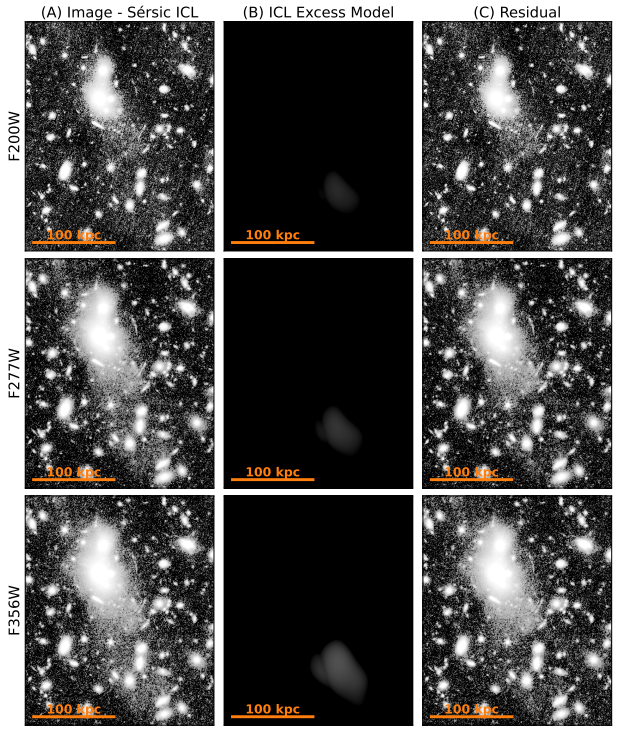


**Figure 4.** Localization of non-Sérsic diffuse emission in XLSSC 122. The left column presents JWST/NIRCam images (F200W, F277W, and F356W) following the subtraction of the best-fit 2D Sérsic ICL (diffuse) component, revealing a prominent residual signal to the south. The middle column displays the isolated model of this additional diffuse component as detected by the wavelet-based algorithm `DAWIS`. The right column shows the final residual maps after subtracting both the global Sérsic and local `DAWIS` models. This southern feature represents a significant excess of diffuse emission extending approximately 100 kpc from the BCG. Its spatial alignment with the overdensity of member galaxies and independent multiwavelength asymmetries (X-ray, radio, and SZ) strongly suggests an origin in tidally stripped stars resulting from ongoing or recent dynamical interactions within the cluster.

While this value, if entirely originating from stripping, is lower than the average stripping contribution predicted by theoretical models, it is not unreasonably small when considering the

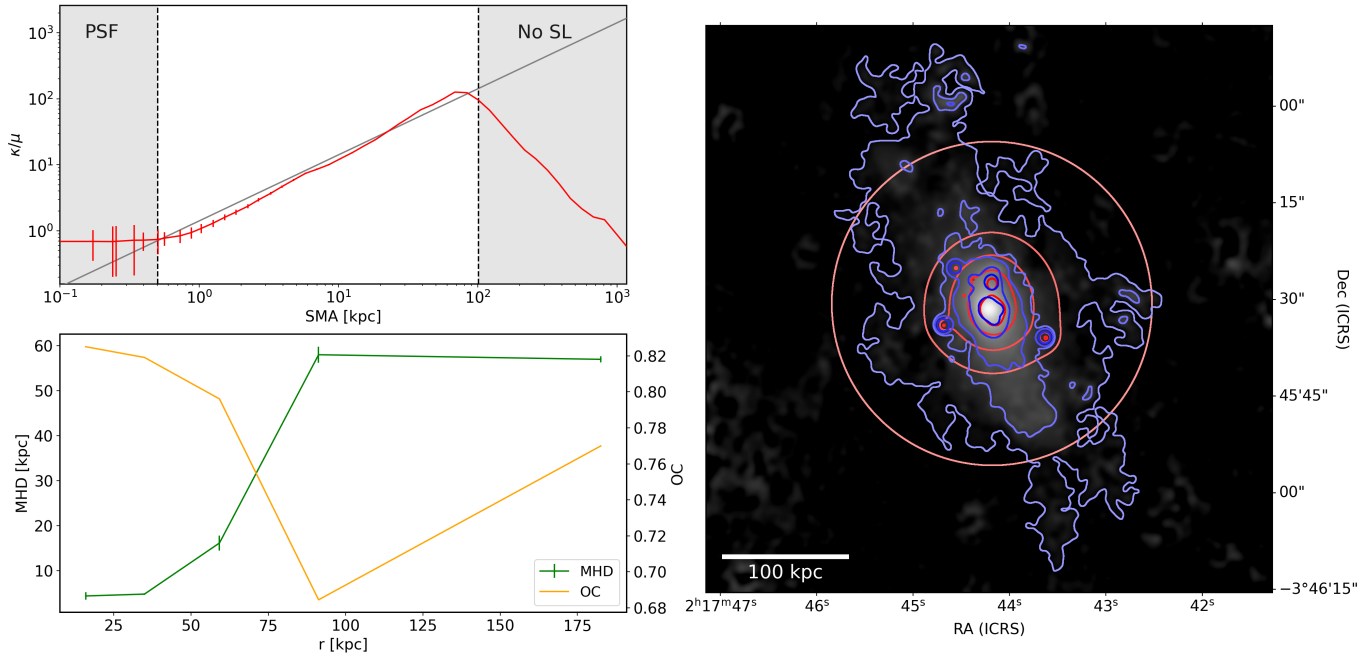


**Figure 5.** Comparison between the mass distribution and diffuse stellar light in XLSSC 122. Top left: the radial profile of the mass-to-light ratio ($\kappa/\mu$) is derived from the SL mass map and the F356W SB profile. The ratio follows a linear relation ($\kappa/\mu \propto r$) up to $r \sim 100$ kpc, the regime where the SL model constraints are most robust. Right: a 2D comparison between the SL mass distribution (red contours) and the smoothed stellar light distribution of the combined BCG + ICL + lens galaxies adopted in K. Finner et al. (2025, blue contours and gray scales) is presented. Bottom left: the orange curve illustrates the overlap coefficient (OC) between the light and mass contours, while the green curve displays the modified Hausdorff distance (MHD). Both metrics consistently indicate that the overall morphological similarity between the mass and diffuse light components remains high out to $r \sim 100$ kpc, while the behavior at larger radii should be interpreted with caution. The slight decrease in similarly beyond $r \sim 60$ kpc is attributed to the presence of the southern ICL excess and the lack of the SL constraints.

expected cluster-to-cluster variations. Rather than indicating a fundamental inconsistency, this difference likely reflects the fact that the observed excess traces only a subset of the total stripped component. In particular, our modeling may miss more smoothly distributed or dynamically mixed stripped stars, and thus the detected excess should not be interpreted as representing all stripping events. Nevertheless, the presence of this localized ICL feature provides evidence for ongoing or recent interactions among cluster member galaxies. This asymmetric excess provides additional observational support that XLSSC 122 is dynamically disturbed, as inferred directly from its ICL.

In addition to the diffuse optical excess, independent multiwavelength datasets show consistent signatures of asymmetry along the same axis. X-ray imaging reveals an elongated morphology aligned with the asymmetric ICL (A. B. Mantz et al. 2014), and radio observations (M. Jarvis et al. 2016; C. L. Hale et al. 2025) show a peak located near this overdense region (Z. P. Scofield et al. 2026). Furthermore, the S/N peak of the SZ effect is observed near the location of the asymmetric ICL feature (J. van Marrewijk et al. 2023), suggesting the presence of bulk gas motions or ongoing interactions. These multiwavelength indications collectively support the interpretation that the southern diffuse component originates from recent or ongoing dynamical activity within the cluster. For a more detailed comparison, including X-ray, radio, and SZ analyses, readers are referred to Z. P. Scofield et al. (2026).

### *4.3. Comparison with Strong-lensing Mass*

To assess the connection between the ICL and the cluster potential, we compared the mass distribution with the BCG + ICL light distribution. This offers a direct observational test of whether the BCG + ICL light distribution traces the SL mass distribution at $z \sim 2$. Recently, J. Yoo et al. (2024) and J. Butler et al. (2025) found that the dark matter to BCG + ICL density ratio profile is an approximately linear function of radius. This relation may be the result of differences between the underlying physics of dark-matter assembly and baryonic evolution. In the CDM paradigm, baryons undergo radiative cooling and energy dissipation to form highly concentrated stellar components at galaxy scales, whereas dark matter remains as an extended, collisionless halo. Within the cluster potential, the stellar and dark-matter components of a galaxy are redistributed differently because of their distinct internal binding energy distributions. This leads to a BCG + ICL distribution that is more centrally concentrated than the dark-matter profile.

The top left panel of Figure 5 shows the lensing mass profile $\kappa(r)$ divided by the BCG + ICL SB profile $\mu(r)$. This profile is constructed using the F356W band, which provides the strongest BCG + ICL signal and the deepest radial extent. The innermost region of the SB profile ($\sim$0.6 kpc) is artificially flattened by the PSF. Beyond this radius, the ratio $\kappa/\mu$ scales approximately linearly with radius ($\kappa/\mu \propto \sim r$), consistent with the $r$ dependence reported in previous studies. This scaling breaks down beyond $\sim$100 kpc, where the SL constraints become sparse due to the rapid decline in the number of multiple images. This radius also coincides with the southern ICL excess identified in Section 4.2, further complicating the comparison between the mass and light distributions.

We also compared the 2D morphological similarity between the BCG + ICL and the SL mass distribution from K. Finner et al. (2025). The BCG and ICL are known to follow the

cluster dark-matter distribution (M. Montes & I. Trujillo 2019; J. M. Diego et al. 2023; S. Cha et al. 2025). To make this comparison, we constructed a 2D light distribution by first masking all detected sources except for the galaxies used in the construction of the SL mass map (K. Finner et al. 2025) in the same manner as in Section 2.2. Then, we filled the masked area with a composite model consisting of the triple-Sérsic model from Section 3.1 and the southern excess model described in Section 4.2, and applied a Gaussian smoothing kernel with $\sigma = 25$ pixels to enhance the large-scale flux distribution. The background of the right panel in Figure 5 shows the BCG, ICL, and galaxy flux distribution used for comparison with the mass distribution.

To quantify the above morphological similarities, we use the weighted OC (WOC; J. Yoo et al. 2022). The WOC evaluates the similarity of two contour sets by measuring the area of the overlapping regions, yielding higher values for greater similarities. The two contour sets that we used are displayed in the right panel of Figure 5. The red contours are from the SL mass map and the blue contours are from BCG + ICL + galaxies. The orange line in the lower left panel of Figure 5 shows the OC at each radius.[11] The OC value at the central region ($r \sim 20$ kpc) was about 0.82, indicating that the BCG + ICL distribution closely traces the mass in the inner halo. Farther from the center, the OC value slightly decreases, reaching 0.78 at $r \sim 60$ kpc. This decline is expected given the ellipticity mismatch between the mass and ICL distributions in this region. Nevertheless, the level of overall agreement at $r \lesssim 60$ kpc remains high. The similarity drops more steeply beyond $r \gtrsim 60$ kpc, reaching OC $\sim 0.69$ at $r \sim 100$ kpc. At this radius, we find an excess of ICL on the southern side of the BCG (Section 4.2), which is not present in the mass map. Beyond this southern excess region, the agreement increases again (OC $\sim 0.77$ at $r \sim 180$ kpc). However, this outer-radius behavior should be interpreted with caution, since the SL constraints become less robust. The WOC value (i.e., the weighted average of all OC values) is 0.813, indicating a high level of agreement between the overall light and mass distributions.

In addition to the WOC, we also employed the MHD (M.-P. Dubuisson & A. K. Jain 1994) to quantify the comparison, where lower values indicate higher similarities. We used the same set of contours adopted for the WOC calculation. The green line in the lower left panel of Figure 5 shows the resulting MHD values. The mean MHD value is ~28.1 kpc. The MHD result is highly consistent with the OC trend, showing high similarity in the inner region and low similarity beyond ~100 kpc.

Overall, the OC and MHD show that the BCG + ICL closely follows the SL mass map at $r \lesssim 100$ kpc, providing direct observational evidence that the stellar distribution traces the cluster potential at $z \sim 2$. The reduced agreement at larger radii likely reflects the sparsity of multiple image constraints, or mismatch between the diffuse stellar light and dark-matter distributions in an unrelaxed system (J. Yoo et al. 2024). In this context, weak lensing extends the comparison to larger scales, showing improved agreement around $r \gtrsim 100$ kpc (Z. P. Scofield et al. 2026). Moreover, the linear regime of $\kappa/\mu$ extends from ~100 kpc in the SL comparison to ~200 kpc when $\kappa(r)$ is taken from the weak-lensing reconstruction.

[11] WOC is the weighted average of OC values at all radii.

## 5. Summary

In this work, we analyzed the ICL in XLSSC 122 at $z = 1.98$ and detected diffuse emission extending to several hundred kiloparsecs from the BCG. The diffuse signal is strong in the rest-frame optical but fainter in the ultraviolet, consistent with an evolved stellar population dominating the diffuse components.

The SB profiles require three components: a compact BCG core, an extended BCG envelope, and an ICL component. This decomposition is stable across all filters, with broadly similar Sérsic indices. The overall color profiles are flat, implying minimal radial variation in the dominant stellar populations of the BCG envelope and the ICL.

The ICL fraction varies across the filters, with a mean value of 16.8%. Notably, this fraction peaks near 4800 Å in the rest frame, a behavior that closely mirrors the trends observed in dynamically active clusters at much lower redshifts.

We also detected a significant ICL excess $\gtrsim$100 kpc south of the BCG in F200W, F277W, and F356W. Its location coincides with the southern overdensity in the member galaxy distribution and is consistent with the asymmetry seen in X-rays, SZ, and radio. This excess emission contributes ~4% of the total ICL flux and may be attributed to tidal stripping from galaxy interactions.

Within ~100 kpc, the BCG + ICL distribution follows the cluster mass (WOC $\sim 0.813$, MHD $\sim 28$ kpc), and the $\kappa/\mu$ profile linearly increases with radius. This indicates that the ICL can trace the dark-matter distribution even in the $z \sim 2$ regime. Taken together, our results demonstrate that a mature yet still growing ICL component was already present in a $M_{200} > 10^{14} M_{\odot}$ halo at $z \sim 2$.

## Acknowledgments

This work is based on observations made with the NASA/ESA/CSA JWST and downloaded from the Mikulski Archive for Space Telescopes (MAST) at the Space Telescope Science Institute (STScI), which is operated by the Association of Universities for Research in Astronomy, Inc., under NASA contract NAS 5-03127 for JWST. These observations are associated with program #3950. Support for program #3950 was provided by NASA through a grant from the Space Telescope Science Institute, which is operated by the Association of Universities for Research in Astronomy, Inc., under NASA contract NAS 5-03127. The HST and JWST data presented in the Letter were obtained from MAST at STScI. The observations can be accessed via DOI: 10.17909/16ah-g805. H.J. acknowledges support from the International Joint Research Grant of Yonsei Graduate School. M.J.J. acknowledges support for the current research from the National Research Foundation (NRF) of Korea under the programs 2022R1A2C1003130 and RS-2023-00219959. B.L. is supported by the NRF grant funded by the Korea government (MSIT), 2022R1C1C1008695.

## Author Contributions

H.J. led the ICL analysis, reduced the HST and JWST data, estimated photometric redshifts, and wrote the paper. M.J.J. supervised the project and contributed to manuscript writing. Z.S. assisted with the JWST/NIRCam data reduction and participated in the interpretation of the results. J.K. assisted

with the HST data reduction. K.F. and S.C. provided the SL results and participated in the interpretation.

## Appendix A
## Customized Data Reduction

### A.1. 1/f Noise Correction

The images taken with NIRCam are known to suffer from $1/f$ noise. This is correlated read noise from the NIRCam detector readout system, caused by the readout integrated circuits and the direct current bias in the SIDECAR ASIC electronics (E. Schlawin et al. 2020). An example of this noise is shown in Figure 6(a), where horizontal and vertical stripe patterns are visible. The horizontal stripes form four distinct bands corresponding to the detector readout structure, whereas the vertical stripes extend uniformly across the image.

To mitigate the $1/f$ noise, we first estimated the horizontal noise. We divided the original $2048 \times 2048$ image into four subimages of size $2048 \times 512$, following the readout structure, and estimated the horizontal noise for each subimage. Then we computed the derivatives along each vertical line. Due to the correlated noise, the derivatives also exhibited characteristic stripe patterns corresponding to the horizontal noise structure. We estimated the median derivative value at each row and subtracted it from the derivative images. To reconstruct the image, we integrated the derivative field in the vertical direction using the first row of each original subimage as the reference. Then, we combined the four horizontally denoised subimages. We estimated the vertical noise with a similar procedure but without dividing the image into subimages.

Figure 6(b) shows the total $1/f$ noise for an example NIRCam exposure modeled in this work. Figure 6(c) shows the denoised image obtained by subtracting the total noise from the original image. This method allows us to measure the $1/f$ noise with much less influence from extended low SB features such as the ICL compared to measuring it directly from the original image. For comparison, Figures 6(d) and (e) show the $1/f$ noise estimate and the corresponding denoised image produced by the default JWST pipeline. Figure 6(f) shows the difference between our result (Figure 6(c)) and the default JWST pipeline output (Figure 6(e)), revealing a nonnegligible feature left by the default pipeline. This motivates our customized correction, which more effectively suppresses the detector correlated stripes while minimizing contamination from extended low SB emission.

### A.2. Sky Gradients and Background Correction

Before mosaicking the final data, we corrected the sky gradient and background for each exposure. To measure the sky gradient, we adopted a linear plane model described by the following equation:

$$I_{\rm sky}(x, y) = ax + by + c. \tag{A1}$$

The coefficients $a$, $b$, and $c$ in Equation (A1) represent the gradients along the $x$- and $y$-directions and the total level of the sky, respectively. The $x$- and $y$-values correspond to pixel coordinates ranging from 0 to 2047. For each observation, we optimized the plane model to estimate $a$, $b$, and $c$. To suppress contamination from astronomical sources, we masked regions brighter than the 68th percentile of the overall pixel-value distribution. This threshold was chosen to systematically exclude pixels dominated by stars, galaxies, or diffuse emission, thereby minimizing bias in the estimation of the sky gradient. The fitted sky model was then subtracted from each image to remove large-scale linear gradients. Although this correction is small ($\sim$0.1% at 29 mag arcsec$^{-2}$), we applied the correction to ensure an accurate measurement of the diffuse ICL component.

Next, we subtracted the residual sky background after mosaicking images. To mask bright astronomical objects, we adopted the segmentation map generated by `SExtractor` as a base mask map. Then we expanded the mask following

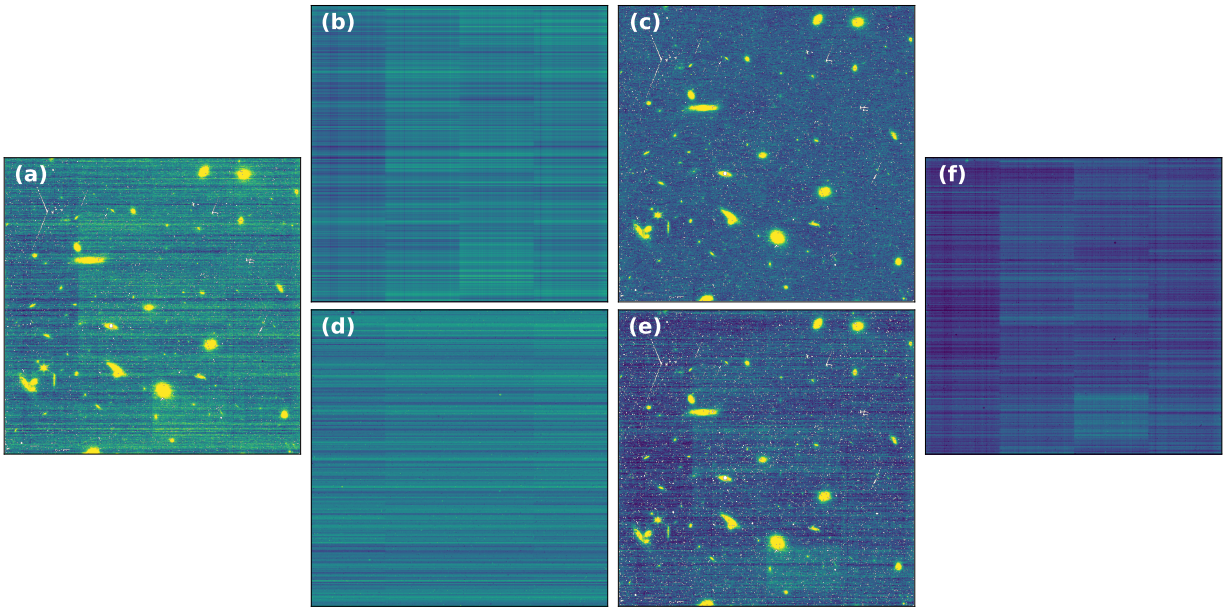


**Figure 6.** Example of modeling the $1/f$ noise. Panel (a) shows the original image. Panels (b) and (c) present, respectively, the modeled $1/f$ noise and the denoised image obtained with our algorithm described in Appendix A.1. Panels (d) and (e) show the output of the JWST pipeline algorithm (`clean_flicker_noise`). Panel (f) illustrates the difference between the two algorithms. Our algorithm effectively avoids overcorrection near bright sources and better preserves diffuse emission.

**Table 1**
Exposure Times and Limiting Surface Brightnesses

| Filter | Exposure Time (s) | $\mu_{\rm lim}$ (mag arcsec$^{-2}$) |
|---|---|---|
| HST/F814W | 17,056.0 | 28.1 |
| HST/F105W | 2611.8 | 28.5 |
| HST/F140W | 5170.5 | 28.4 |
| JWST/F090W | 7558.6 | 29.5 |
| JWST/F200W | 4208.8 | 28.8 |
| JWST/F277W | 7558.6 | 29.2 |
| JWST/F356W | 4208.8 | 29.1 |

Equation (1). We found that the estimated sky background converges when $c_{\rm e}$ is greater than or equal to 2.0, which corresponds to a more conservative masking choice that prioritizes maximal contamination removal. Therefore, we adopted the sky background measured at $c_{\rm e} = 2.0$ for the final correction. Although the constant term $c$ in Equation (A1) already removes the first-order sky level, neglecting this additional correction introduces an error of about 0.03% at 29 mag arcsec$^{-2}$ .

We derived the SB limits $\mu_{\rm lim}$ for each band by measuring the standard deviation of the sky pixel-value distribution within a masked background region. This region was defined outside the 1 Mpc ellipse (SMA $\approx 119''$; Section 2.2) and covers a total area of $\sim$1 arcmin$^2$. The resulting $\mu_{\rm lim}$ values for all bands are summarized in Table 1.

To account for systematic uncertainties in the sky estimation $\sigma_{\rm sky}$, we divided the background region into 20 azimuthal bins and measured the median sky value within each bin. We then adopted the standard deviation of these 20 mean values as the characteristic sky estimation error $\sigma_{\rm sky}$. This systematic error is incorporated into the error propagation for all subsequent SB measurements.

## Appendix B
## Cluster Member Selection

Previous spectroscopic analyses identified 50 cluster member galaxies in the XLSSC 122 field (J. P. Willis et al. 2020). We now have seven-band photometry from HST and JWST, which can aid in cluster member identification further. Photometric measurements were performed in the dual-image mode of `SExtractor` (E. Bertin & S. Arnouts 1996), where a detection image was created by combining the four JWST filters, and fluxes were measured in all seven bands. Photometric redshifts were then estimated with `eazy-py` (G. B. Brammer et al. 2008).

Since the cluster lies at $z \sim 2$, distinguishing background galaxies from cluster members becomes nontrivial. At these redshifts, photometric redshift uncertainties are relatively high due to the limited wavelength coverage of the key spectral features and the degeneracy between redshift, dust extinction, and stellar population age. Moreover, the SEDs of high-redshift galaxies can differ from those of low-redshift counterparts, as they are often dominated by younger stellar populations, higher star formation rates, and stronger dust attenuation. To improve the robustness of our member identification, we adopted the high-redshift optimized SED templates from R. L. Larson et al. (2023), which are optimized for high-redshift photometric redshift fitting and can reduce

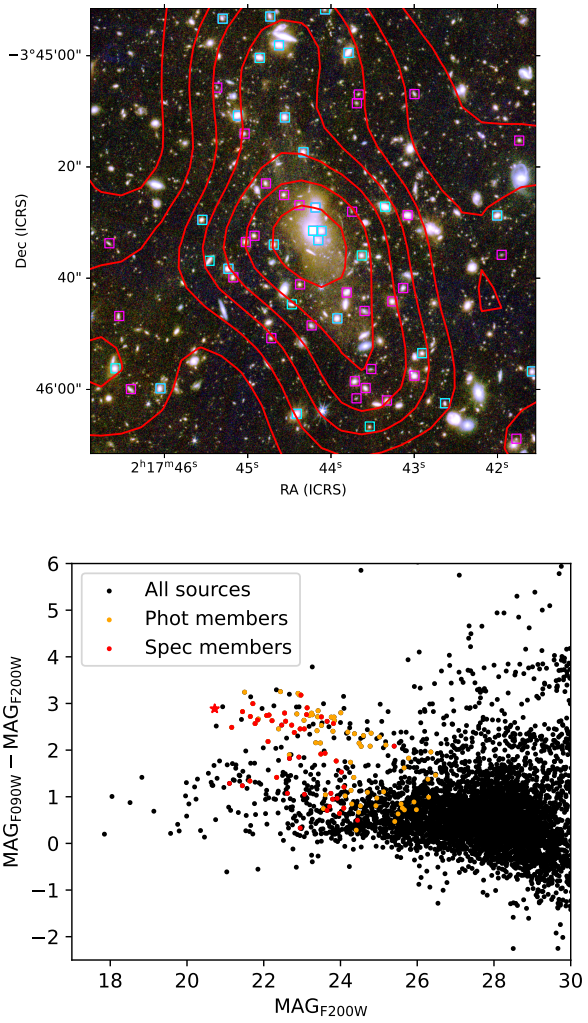


**Figure 7.** Top: color-composite image of XLSSC 122 with red for F356W, green for F277W, and blue for F090W + F200W. The cyan boxes indicate spectroscopically confirmed member galaxies and magenta boxes show photometric members. The red contours show the smoothed number density distribution of all known member galaxies. Bottom: color–magnitude diagram of the JWST XLSSC 122 field. Black dots indicate all detected sources. Red and orange dots show spectroscopically and photometrically selected member galaxies, respectively. The star represents the BCG.

low-redshift interloper solutions, and may help mitigate contamination in member selection.

Using the photometric redshift of each source and its associated uncertainty, we selected only those with uncertainties smaller than 25%. The range of selected member candidates lies at $1.7 \lesssim z_{\rm phot} \lesssim 2.3$. We then used the spectroscopic catalog of J. P. Willis et al. (2020) to remove spectroscopically confirmed foreground objects and to retain 50 confirmed cluster members. After this spectroscopic cleaning, our photometric selection contains 90 member candidates, of which 60 are newly identified in this work. For the 30 sources with both photometric and spectroscopic redshifts, we find good agreement, with $|z_{\rm phot} - z_{\rm spec}|/(1 + z_{\rm spec}) < 0.1$.

In the top panel of Figure 7, cyan boxes mark spectroscopically confirmed members, while magenta boxes denote photometric members. The distribution of member galaxies is centered around the BCG and shows an elongated morphology along the north–south direction, with a pronounced extension toward the south. This elongation is aligned with the major

axis of the BCG and the ICL in XLSSC 122 measured in Section 2.2. As shown in the bottom panel of Figure 7, the distribution of these members in the color–magnitude diagram exhibits a well-defined red sequence. In addition to the red members, we also identified a blue population, consistent with ongoing star formation activity. These photometric member distributions in the bottom panel of Figure 7 are consistent with those found in J. P. Willis et al. (2020), and they extend to sources up to 2 mag fainter than the spectroscopic members.

## ORCID iDs

Hyungjin Joo https://orcid.org/0000-0001-9139-5455
M. James Jee https://orcid.org/0000-0002-5751-3697
Kyle Finner https://orcid.org/0000-0002-4462-0709
Zachary P. Scofield https://orcid.org/0009-0009-4086-7665
Sangjun Cha https://orcid.org/0000-0001-7148-6915
Jinhyub Kim https://orcid.org/0000-0003-2776-2761
Ranga-Ram Chary https://orcid.org/0000-0001-7583-0621
Andreas Faisst https://orcid.org/0000-0002-9382-9832
Bomee Lee https://orcid.org/0000-0003-1954-5046

## References

Bertin, E., & Arnouts, S. 1996, A&AS, 117, 393
Brammer, G. B., van Dokkum, P. G., & Coppi, P. 2008, ApJ, 686, 1503
Brown, H. J., Martin, G., Pearce, F. R., et al. 2024, MNRAS, 534, 431
Buchner, J., Georgakakis, A., Nandra, K., et al. 2014, A&A, 564, A125
Bushouse, H., Eisenhamer, J., Dencheva, N., et al. 2022, JWST Calibration Pipeline, v1.8.2, doi:10.5281/zenodo.7229890
Butler, J., Martin, G., Hatch, N. A., et al. 2025, MNRAS, 539, 2279
Cha, S., Cho, B. Y., Joo, H., et al. 2025, ApJL, 987, L15
Chun, K., Shin, J., Ko, J., Smith, R., & Yoo, J. 2024, ApJ, 969, 142
Contini, E., Chen, H. Z., & Gu, Q. 2022, ApJ, 928, 99
Contini, E., De Lucia, G., Villalobos, A., & Borgani, S. 2014, MNRAS, 437, 3787
Contini, E., Rhee, J., Han, S., Jeon, S., & Yi, S. K. 2024, AJ, 167, 7
Contini, E., Yi, S. K., & Kang, X. 2019, ApJ, 871, 24
Coogan, R. T., Daddi, E., Le Bail, A., et al. 2023, A&A, 677, A3
de Oliveira, N. O. L., Jiménez-Teja, Y., & Dupke, R. 2022, MNRAS, 512, 1916
de Oliveira, N. O. L., Jiménez-Teja, Y., Dupke, R. A., et al. 2025, ApJL, 988, L45
Deason, A. J., Oman, K. A., Fattahi, A., et al. 2021, MNRAS, 500, 4181
DeMaio, T., Gonzalez, A. H., Zabludoff, A., et al. 2018, MNRAS, 474, 3009
Diego, J. M., Pascale, M., Frye, B., et al. 2023, A&A, 679, A159
Dubuisson, M.-P., & Jain, A. K. 1994, in Proc. 12th IAPR Int. Conf. Pattern Recognition, 1, (IEEE), 566
Ellien, A., Slezak, E., Martinet, N., et al. 2021, A&A, 649, A38
Finner, K., Cha, S., Scofield, Z. P., et al. 2025, ApJL, 994, L35
Gonzalez, A. H., George, T., Connor, T., et al. 2021, MNRAS, 507, 963
Hale, C. L., Heywood, I., Jarvis, M. J., et al. 2025, MNRAS, 536, 2187
Hoffmann, S. L., Mack, J., Avila, R., et al. 2021, AAS, 53, 216
Jarvis, M., Taylor, R., Agudo, I., et al. 2016, in MeerKAT Science: On the Pathway to the SKA, 6
Jee, M. J. 2010, ApJ, 717, 420
Jeffreys, H. 1998, The Theory of Probability, Oxford Classic Texts in the Physical Sciences (Oxford Univ. Press), 432
Jeon, S., Contini, E., Han, S., et al. 2026, ApJ, 998, 30
Jiménez-Teja, Y., & Dupke, R. 2016, ApJ, 820, 49
Jiménez-Teja, Y., Dupke, R., Benítez, N., et al. 2018, ApJ, 857, 79
Jiménez-Teja, Y., Dupke, R. A., Lopes, P. A. A., & Dimauro, P. 2024, ApJL, 960, L7
Jiménez-Teja, Y., Román, J., HyeongHan, K., et al. 2025, A&A, 694, A216
Jiménez-Teja, Y., Vílchez, J. M., Dupke, R. A., et al. 2021, ApJ, 922, 268
Joo, H., & Jee, M. J. 2023, Natur, 613, 37
Joo, H., Jee, M. J., Kim, J., et al. 2025, ApJ, 990, 96
Kim, J., Jee, M. J., Andreon, S., et al. 2025, ApJ, 991, 109
Kimmig, L. C., Brough, S., Dolag, K., et al. 2025, A&A, 700, A95
Ko, J., & Jee, M. J. 2018, ApJ, 862, 95
Krist, J. E., Hook, R. N., & Stoehr, F. 2011, SPIE, 8127, 81270J
Larson, R. L., Hutchison, T. A., Bagley, M., et al. 2023, ApJ, 958, 141
Mantz, A. B., Abdulla, Z., Allen, S. W., et al. 2018, A&A, 620, A2
Mantz, A. B., Abdulla, Z., Carlstrom, J. E., et al. 2014, ApJ, 794, 157
Matheron, G. 1988, in Image Analysis and Mathematical Morphology, ed. J. P. Serra, Vol. 1 (Academic Press), 59
Mayes, R. J., Gómez, F. A., & Monachesi, A. 2026, A&A, 708, A124
Montes, M., & Trujillo, I. 2017, MNRAS, 474, 917
Montes, M., & Trujillo, I. 2019, MNRAS, 482, 2838
Murante, G., Giovalli, M., Gerhard, O., et al. 2007, MNRAS, 377, 2
Noordeh, E., Canning, R. E. A., Willis, J. P., et al. 2021, MNRAS, 507, 5272
Perrin, M. D., Sivaramakrishnan, A., Lajoie, C.-P., et al. 2014, SPIE, 9143, 91433X
Pierre, M., Pacaud, F., Adami, C., et al. 2016, A&A, 592, A1
Pierre, M., Pacaud, F., Duc, P. A., et al. 2006, MNRAS, 372, 591
Rudick, C. S., Mihos, J. C., Frey, L. H., & McBride, C. K. 2009, ApJ, 699, 1518
Rudick, C. S., Mihos, J. C., & McBride, C. 2006, ApJ, 648, 936
Schlawin, E., Leisenring, J., Misselt, K., et al. 2020, AJ, 160, 231
Scofield, Z. P. 2025, young-jwstpipe: JWST data calibration pipeline, v1.0, Zenodo, doi:10.5281/zenodo.16961663
Scofield, Z. P., Finner, K., Joo, H., et al. 2026, ApJL, 999, L1
Sérsic, J. L. 1963, BAAA, 6, 41
Shi, D. D., Wang, X., Zheng, X. Z., et al. 2024, ApJ, 963, 21
Shimakawa, R., Koyama, Y., Kodama, T., et al. 2025, MNRAS, 537, L36
Stone, C. J., Arora, N., Courteau, S., & Cuillandre, J.-C. 2021, MNRAS, 508, 1870
Sun, H., Wang, T., Xu, K., et al. 2024, ApJL, 967, L34
Sunnquist, B., Boyer, M., Brooks, B., et al. 2024, Improved NIRCam Flat Field Reference Files for Cycle 1, JWST Technical Report JWST-STScI-008607, Space Telescope Science Institute (STScI)
van Marrewijk, J., Mroczkowski, T., & Di Mascolo, L. 2023, ALMA at 10 years: Past, Present, and Future, v1, Zenodo, doi:10.5281/zenodo.10203327
Werner, S. V., Hatch, N. A., Matharu, J., et al. 2023, MNRAS, 523, 91
Willis, J. P., Canning, R. E. A., Noordeh, E. S., et al. 2020, Natur, 577, 39
Willis, J. P., Clerc, N., Bremer, M. N., et al. 2013, MNRAS, 430, 134
Yoo, J., Ko, J., Sabiu, C. G., et al. 2022, ApJS, 261, 28
Yoo, J., Park, C., Sabiu, C. G., et al. 2024, ApJ, 965, 145
Zhang, Y., Yanny, B., Palmese, A., et al. 2019, ApJ, 874, 165
Zwicky, F. 1937, ApJ, 86, 217